Chinese Physics Letters

LETTER

Circular Phonon Dichroism in d-Wave Altermagnets

Cite as: Ding Li *et al*. 2026 *Chin. Phys. Lett.* **43** 110709

DOI CSTR

Recommended Articles

Probing the Néel Order in Altermagnetic RuO_2 Films via X-Ray Magnetic Linear Dichroism

Yi-Chi Zhang *et al*.
Chin. Phys. Lett. **42**, 027301 (2025)

Spin Quadrupolar Order in d-wave Unconventional Magnetism

Jian-Keng Yuan, Zhiming Pan, and Congjun Wu
Chin. Phys. Lett. **43**, 090703 (2026)

Symmetry-Constrained Anomalous Transport in the Altermagnetic Material CuX_2 (X = F, Cl)

Zhengxuan Wang, Ruqian Wu, Chunlan Ma, Shijing Gong, Chuanxi Zhao, Shuaikang Zhang, Guangtao Wang, Tianxing Wang, and Yipeng An
Chin. Phys. Lett. **42**, 080705 (2025)

Magnon Splitting and Magnon Spin Transport in Altermagnets

Kun Wu, Jianting Dong, Meng Zhu, Fanxing Zheng, and Jia Zhang
Chin. Phys. Lett. **42**, 070702 (2025)

Tunneling Magnetoresistance Effect in Altermagnetic Tunnel Junctions with g-Wave Splitting

Xinlu Li, Meng Zhu, Jianting Dong, Kun Wu, Fanxing Zheng, and Jia Zhang
Chin. Phys. Lett. **42**, 100701 (2025)

ARPES Studies of Spin-Splitting Antiferromagnets

Xinnuo Zhang, Jiayu Liu, Wencheng Huang, Fayuan Zhang, Ming-Yuan Zhu, Yu-Peng Zhu, Chaoyu Chen, Chang Liu, Changyoung Kim, and Dawei Shen
Chin. Phys. Lett. **43**, 050709 (2026)

A series journal of Chinese Physical Society distributed by IOP Publishing

Chinese Physics Letters

Chin. Phys. Lett. **43** 110709 (2026)

LETTER

DOI: 10.1088/0256-307X/43/11/110709
CSTR: 32039.14.0256-307X.43.11.110709

Circular Phonon Dichroism in d-Wave Altermagnets

Ding Li(李顶)[1,2], Tao Qin(秦涛)[3], and Jianhui Zhou(周建辉)[1,*]

[1]Anhui Key Laboratory of Low-Energy Quantum Materials and Devices, High Magnetic Field Laboratory, Hefei Institutes of Physical Science, Chinese Academy of Sciences, Hefei 230031, China
[2]Department of Physics, University of Science and Technology of China, Hefei 230026, China
[3]School of Physics, Anhui University, Hefei 230601, China

[*]Corresponding author. Email: jhzhou@hmfl.ac.cn

Altermagnets, a new class of collinear antiferromagnets, exhibit momentum-dependent spin splitting and offer compelling advantages for antiferromagnetic spintronics. However, the magnetic order is intrinsically difficult to read out, which hinders practical applications. We propose finite-momentum circular phonon dichroism (CPD) as a direct probe that distinguishes the two opposite out-of-plane Néel vector configurations in two-dimensional d-wave altermagnets. Combining Onsager reciprocity with C_{2z} lattice symmetry, we find that the dichroic signal reverses sign when the Néel vector is flipped for the in-plane phonon wave vectors. Moreover, a channel-resolved decomposition identifies the CPD originates from the interband coherent transitions. Representative finite-momentum cuts show pronounced dichroic asymmetric ratio, with $|\eta_{\mathrm{CPD}}| = 36\%$. Our work reveals that the circular-ultrasound absorption can distinguish the two opposite out-of-plane Néel vector configurations of d-wave altermagnets.

Introduction

Antiferromagnets offer several advantages over ferromagnets for information storage: absence of stray fields, terahertz-scale spin dynamics, and vanishing net magnetization [1–4]. Altermagnets, a new class of collinear antiferromagnets with momentum-dependent spin splitting [5–9], have attracted significant attention not only for their remarkable functionalities, including the electrical spin-splitter effect, giant and tunneling magnetoresistance, and spin-splitting torque [10–13], but also as an ideal platform for exploring many novel physical effects [14–29]. However, determining the orientation of the Néel vector remains a major challenge [30–35]. Since the spin splitting and associated electronic wave functions depend sensitively on the Néel order, reversing the Néel vector modifies the underlying electronic structure and its quantum-geometric properties [36–39], providing a powerful route for detecting the Néel vector in altermagnetic materials.

Circularly polarized phonons can carry angular momentum and chirality [40–42], and phonon dichroism has been proposed as finite-momentum probes of electronic dissipation in several quantum materials [43,44]. It has been shown that both linear and circular phonon dichroism (CPD) can reveal the electronic quantum geometry through electron–phonon coupling [45]. These findings naturally suggest that phonon dichroism may also encode information about the Néel vector orientation through its influence on the electronic quantum geometry [46–49]. Moreover, phonons intrinsically carry finite momentum, enabling momentum-resolved probes of electronic dissipation beyond the long-wavelength regime, particularly the anisotropic spin-splitting Fermi surface in altermagnets.

In this work, we develop a theory of finite-momentum phonon absorption and demonstrate that CPD provides a direct signature of the two opposite out-of-plane Néel vector domains in metallic d-wave altermagnets. Combining Onsager reciprocity with C_{2z} symmetry, we find that the dichroic signal reverses sign when the Néel vector is flipped for in-plane phonon wave vectors. A channel-resolved decomposition identifies the interband coherent origin of the CPD. Numerical calculations for d-wave altermagnets reveal strong modulation of the CPD near the resonant finite wave vector.

Formalism of Phonon Dichroism

The total Hamiltonian contains ionic, electronic, and electron–phonon parts, $H_{\mathrm{tot}} = H_{\mathrm{ion}} + H_{\mathrm{el}} + H_{\mathrm{e\text{–}ph}}$ [50]. To linear order in the ionic displacement $\boldsymbol{u}(\boldsymbol{q})$, the electron–phonon coupling is $H_{\mathrm{e\text{–}ph}} = -\sum_{\boldsymbol{q},\alpha} \hat{T}_\alpha(-\boldsymbol{q}) u_\alpha(\boldsymbol{q})$, where $\hat{T}_\alpha(\boldsymbol{q})$ is the generalized force operator. For simplicity, we consider the lattice dynamics of a monatomic lattice with an atomic mass M and employ the ionic equation of motion,

$$M\ddot{u}_\alpha(\boldsymbol{q}) = -M\sum_\beta \Phi_{\alpha\beta}(\boldsymbol{q}) u_\beta(\boldsymbol{q}) + \langle \hat{T}_\alpha(\boldsymbol{q},t)\rangle, \tag{1}$$

where M is the ion mass. The electronic feedback force can be calculated within the linear response regime [51], $\langle \hat{T}_\alpha(\boldsymbol{q},\omega)\rangle_{\mathrm{ind}} = \hbar\sum_\beta \chi_{\alpha\beta}(\boldsymbol{q},\omega) u_\beta(\boldsymbol{q},\omega)$, with the retarded force–force response function

$$\chi_{\alpha\beta}(\boldsymbol{q},\omega) = -\frac{\mathrm{i}}{M\hbar}\int_0^\infty \mathrm{d}t\, \mathrm{e}^{\mathrm{i}(\omega+\mathrm{i}0^+)t} \langle [\hat{T}_\alpha(\boldsymbol{q},t), \hat{T}_\beta(-\boldsymbol{q},0)]\rangle_0, \tag{2}$$

where 0^+ is a positive infinitesimal, and the subscript 0 denotes the expectation value in the unperturbed electronic ground state. Combining these gives the eigenvalue equation of phonons

$$\omega^2 u_\alpha(\boldsymbol{q}) = \sum_\beta \left[\hbar^2 \Phi_{\alpha\beta}(\boldsymbol{q}) + \hbar\chi_{\alpha\beta}(\boldsymbol{q},\omega)\right] u_\beta(\boldsymbol{q}). \tag{3}$$

The first term is the bare ion–ion dynamical matrix in the adiabatic limit; the second term encodes the quantum geometric information from the electronic states through the electron–phonon interaction. The dissipative part of the response function $\chi_{\alpha\beta}$ corresponds to the anti-Hermitian part: $\gamma_{\alpha\beta} = (\mathrm{i}/4\omega)(\chi_{\alpha\beta} - \chi^*_{\beta\alpha})$, and describes phonon absorption—such as in Weyl semimetals and two-dimensional (2D) magnetic Dirac materials [43,44,52]. Meanwhile, its Hermitian part is associated with the molecular Berry curvature for phonons, which plays a key role in the chiral phonons and phonon anomalous transport [42,53–56]. For a phonon polarization $\boldsymbol{\epsilon}$, the absorption coefficient is $\gamma^{\boldsymbol{\epsilon}} = \boldsymbol{\epsilon}^\dagger \gamma \boldsymbol{\epsilon}$. Decomposing γ into symmetric and antisymmetric parts yields

$$\gamma = \begin{pmatrix} \gamma_D + \gamma_{\bar{D}} & \gamma^{\bar{A}} + \mathrm{i}\gamma^A \\ \gamma^{\bar{A}} - \mathrm{i}\gamma^A & \gamma_D - \gamma_{\bar{D}} \end{pmatrix}, \tag{4}$$

Received 14 July 2026; accepted 15 October 2026; published 10 November 2026

© 2026 Chinese Physical Society and IOP Publishing Ltd. All rights, including for text and data mining, AI training, and similar technologies, are reserved.

Check for updates

where $\gamma_D = (\gamma_{xx}+\gamma_{yy})/2$ governs polarization-averaged absorption, $\gamma_{\tilde{D}}$ and γ^A govern linear dichroism, and the Hall-like component $\gamma^A = \mathrm{Im}\,\gamma_{xy}$ governs circular dichroism. Thus, a finite CPD requires breaking of both $\mathcal{T}$ and $\mathcal{PT}$ symmetry. The explicit formulas for the four dissipative components are given in the Supplementary Materials (SM).* For normalized circular polarization vectors $\boldsymbol{\epsilon}^{\mathrm{L/R}} = (1, \pm\mathrm{i})/\sqrt{2}$, one finds $\gamma^{\mathrm{L/R}} = \gamma_D \mp \gamma^A$.

In order to evaluate γ^A explicitly, we need the force operator matrix elements at finite phonon momentum. Strain couples to the electronic momentum through the local frame field [57–60], in which the ionic displacement field $\boldsymbol{u}(\boldsymbol{r})$ enters through the local frame $e_j^\mu = \delta_j^\mu - \partial u_j/\partial r_\mu$ in the long-wavelength limit, and the electron–phonon coupling follows from the Hermitian replacement $\hat{p}_j \to (1/2)(\hat{p}_\mu e_j^\mu + e_j^\mu \hat{p}_\mu)$ in the effective Hamiltonian of Bloch electrons in momentum space, $h(\boldsymbol{k})$, which can usually be obtained from symmetry analysis and first-principles calculations. For a phonon with wave vector $\boldsymbol{q}$ and displacement along α, the matrix elements of the force operator are (see details in SM)

$$T_\alpha^{ss'}(\boldsymbol{k},\boldsymbol{q}) = \mathrm{i}\,\boldsymbol{q}\cdot\left(\boldsymbol{k}+\frac{\boldsymbol{q}}{2}\right)\bar{v}_{ss',\alpha}(\boldsymbol{k},\boldsymbol{q}), \tag{5}$$

where $\bar{v}_{ss',\alpha}(\boldsymbol{k},\boldsymbol{q}) = \langle u_{s,\boldsymbol{k}} \left| \frac{\hat{v}_\alpha(\boldsymbol{k})+\hat{v}_\alpha(\boldsymbol{k}+\boldsymbol{q})}{2} \right| u_{s',\boldsymbol{k}+\boldsymbol{q}} \rangle$ is the finite-$\boldsymbol{q}$-averaged velocity matrix element.

The dissipative part is then

$$\gamma^A(\boldsymbol{q},\omega) = -\frac{1}{2\omega}\sum_{ss'}\int \frac{\mathrm{d}^2\boldsymbol{k}}{\rho(2\pi)^2} F_{s's}(\boldsymbol{k},\boldsymbol{q})\,\mathrm{Im}[S_{ss'}(\boldsymbol{k},\boldsymbol{q})], \tag{6}$$

with $F_{s's} = -\pi[f_s(\boldsymbol{k}) - f_{s'}(\boldsymbol{k}+\boldsymbol{q})]\delta[\varepsilon_{s'}(\boldsymbol{k}+\boldsymbol{q}) - \varepsilon_s(\boldsymbol{k}) - \hbar\omega]$ and $S_{ss'}(\boldsymbol{k},\boldsymbol{q}) = \mathrm{Im}[\bar{v}_{ss',x}\bar{v}^*_{ss',y}]\left[\boldsymbol{q}\cdot(\boldsymbol{k}+\boldsymbol{q}/2)\right]^2$. Here $f_s(\boldsymbol{k})$ is the Fermi–Dirac occupation, $\varepsilon_s(\boldsymbol{k})$ is the band energy, and the typical mass density $\rho = 2.2\times10^{-6}\,\mathrm{kg/m^2}$ for RuO_2 is chosen in this work. The factor $\mathrm{Im}F_{s's}$ enforces energy conservation and ensures that the transition occurs between occupied and empty states.

The essential relation for Néel vector readout follows from time-reversal symmetry and Onsager reciprocity [61]. Under the time-reversal operation $\mathcal{T}$, the Néel order parameter reverses: the real-space staggered exchange field $\sum_i J\delta(\boldsymbol{r}-\boldsymbol{r}_i)\sigma_z$ on the magnetic sublattice flips through $\sigma_z \to -\sigma_z$ at fixed spatial profile, equivalently, $J \to -J$; the phonon momentum changes sign $\boldsymbol{q} \to -\boldsymbol{q}$; and the dissipative tensor is transposed $\gamma_{\alpha\beta}(\boldsymbol{q},\omega;J) = \gamma_{\beta\alpha}(-\boldsymbol{q},\omega;-J)$. Taking the imaginary part of the off-diagonal element, $\gamma^A = \mathrm{Im}\,\gamma_{xy}$, gives rise to the Onsager relation

$$\gamma^A(\boldsymbol{q},\omega;J) = -\gamma^A(-\boldsymbol{q},\omega;-J). \tag{7}$$

If the crystal symmetry maps $-\boldsymbol{q}$ back to $\boldsymbol{q}$ while preserving the scalar quantity γ^A, then $\gamma^A(\boldsymbol{q};J) = -\gamma^A(\boldsymbol{q};-J)$, so the CPD changes sign under Néel vector reversal and provides a direct readout of the Néel orientation. Whether this reduction holds depends on the crystal point group. We note that the required momentum mapping is guaranteed for 2D d-wave altermagnets.

We note that CPD can be understood by analogy with photon circular dichroism, such as that probed by X-ray magnetic circular dichroism [62,63]. Specifically, CPD originates from the imaginary part of the phonon-mediated response function, $\mathrm{Im}\,\gamma_{xy}$, whereas photon circular dichroism corresponds to the antisymmetric part of the dynamical anomalous Hall conductivity, $\mathrm{Im}\,\sigma_{xy}$ [64]. Furthermore, a finite CPD requires the electron–phonon coupling to capture both the lattice stretch and rotation. The lattice rotation directly generates chiral phonon modes; the strain $\boldsymbol{u}$ induced by these modes couples to electrons through the elastic gauge vector potential $\hat{\boldsymbol{A}}(\boldsymbol{u})$. The resulting electron–phonon coupling has the form $\hat{H}_{\text{e-ph}} = g\,\hat{\boldsymbol{v}}\cdot\hat{\boldsymbol{A}}(\boldsymbol{u})$, where g is the coupling constant and $\hat{\boldsymbol{v}}$ is the electron velocity operator that induces interband hopping of electrons.

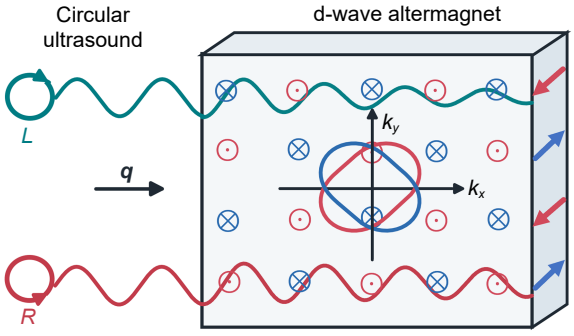

Fig. 1. Dichroic attenuation of circular ultrasound through an altermagnetic material. The red and blue circles denote the local magnetic moments, which are perpendicular to the page and antiparallel to one another. Equal-amplitude left- and right-circular ultrasound waves are transmitted separately through a d-wave altermagnet with a static alternating-spin lattice. The red and blue contours schematically depict the d-wave altermagnetic Fermi surface splitting, which vanishes on the crystalline axes and changes sign between adjacent quadrants. The unequal transmitted amplitudes correspond to $\gamma^{\mathrm{L}} \neq \gamma^{\mathrm{R}}$. At fixed and calibrated $(\boldsymbol{q},\omega)$, the sign of the attenuation difference distinguishes opposite Néel vector orientations.

d-Wave Altermagnets

We focus on the 2D d-wave altermagnet illustrated in Fig. 1, with the Néel vector along the z axis and phonons propagating in the xy plane. Representative material platforms include RuO_2 and KV_2Se_2O [65–68]. Since electron–hole excitations induced by low-energy acoustic phonons (on the meV scale) are greatly suppressed due to the finite band gap, we focus on the metallic case and consider the minimal two-band Hamiltonian for d-wave altermagnets [29,69],

$$h(\boldsymbol{k}) = tk^2\sigma_0 + Jk_xk_y\sigma_z + \lambda(k_x\sigma_y - k_y\sigma_x), \tag{8}$$

where J is the d-wave altermagnetic exchange splitting† and λ is the Rashba spin–orbit coupling (SOC) [70]. The parameters used here are $\mu = 0.4\,\mathrm{eV}$, $t = 2\,\mathrm{eV}$, $\lambda = 0.1\,\mathrm{eV}$, $J = 1.6\,\mathrm{eV}$, $\hbar\omega = 0.002\,\mathrm{eV}$, and $T = 20\,\mathrm{K}$ [17,29,69]. Reversing the Néel vector flips σ_z, which is equivalent to $J \to -J$, since the exchange splitting enters only through $Jk_xk_y\sigma_z$. The Rashba term is essential for the Hall-like response: without it ($\lambda = 0$), the Berry curvature vanishes and γ^A is identically zero [71]. The band dispersion is $\varepsilon_\pm(\boldsymbol{k}) = tk^2 \pm \sqrt{J^2k_x^2k_y^2 + \lambda^2k^2}$. This d-wave exchange splitting vanishes on the crystalline axes and changes sign between adjacent quadrants, producing the alternating spin-split Fermi contours shown in Fig. 1. We note that Rashba SOC is not a general requirement for CPD‡, which could be induced by other forms of SOC or magnon–phonon coupling [72,73].

It is known that 2D d-wave altermagnet retains C_{2z} symmetry [74–76], which maps $\boldsymbol{q} \to -\boldsymbol{q}$ at fixed J while preserving γ^A. Combining C_{2z} with the Onsager relation gives

$$\gamma^A(\boldsymbol{q},\omega;J) \to -\gamma^A(\boldsymbol{q},\omega;-J). \tag{9}$$

This symmetry relation translates into the transmission protocol shown in Fig. 1. At a fixed and calibrated $(\boldsymbol{q},\omega)$, left- and right-circular ultrasound waves with equal incident amplitudes are sent through the sample in separate measurements. Their unequal attenuation yields $\gamma^{\mathrm{L}} \neq \gamma^{\mathrm{R}}$, while reversing the Néel vector $\boldsymbol{n}$ changes the sign of the transmission difference, $\gamma^A(\boldsymbol{n}) = -\gamma^A(-\boldsymbol{n})$. Thus, the readout is a sign-sensitive distinction between the two opposite Néel vector configurations rather than an unconstrained reconstruction of an arbitrary vector direction. Note that the impact of the generic orientation of the Néel vector on $\gamma^A(\boldsymbol{n})$ can be treated analogously to that in transport

*See SM for details of the electron–phonon coupling, force operator, Kubo formula, absorption coefficients, and the numerical results of linear phonon dichroism.

†This is equivalent to the $\boldsymbol{J}$ in the staggered exchange field $\sum_i \boldsymbol{J}\,\delta(\boldsymbol{r}-\boldsymbol{r}_i)\sigma_z$ on the magnetic sublattice.

‡In our 2D model, we adopt the Rashba form because it is the natural SOC for the chosen geometry. Other forms of SOC, such as atomic or Dresselhaus SOC, can play the same role in other settings, including inversion-symmetric crystals.

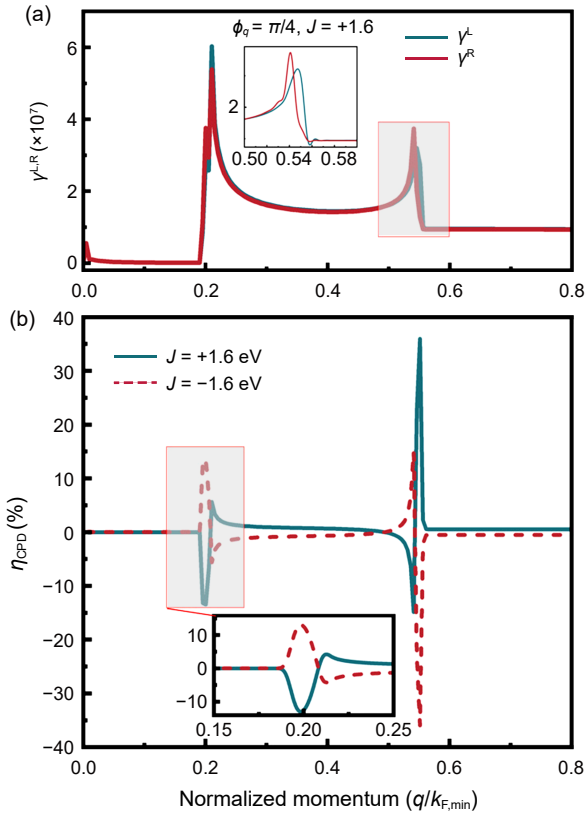

Fig. 2. Radial circular-channel absorption and CPD asymmetry ratio. (a) Momentum dependence of γ^{L} and γ^{R} (in s^{-1}) along $\phi_q = \pi/4$ for $J = 1.6\,\mathrm{eV}$. (b) Normalized CPD asymmetry ratio η_{CPD} along the same direction for $J = \pm 1.6\,\mathrm{eV}$. Solid and dashed curves denote $J = 1.6\,\mathrm{eV}$ and $J = -1.6\,\mathrm{eV}$, respectively. The inset enlarges the low-q resonance region.

properties [11,62].

Figure 2(a) shows the two circular-channel absorptions γ^{L} and γ^{R} at different $\boldsymbol{q}$ along $\phi_q = \pi/4$ for $J = 1.6\,\mathrm{eV}$. They share the same resonant absorption background but separate at selected momenta. Their difference is the CPD and their average gives the polarization-averaged scale γ_{D}. Since the background itself varies strongly with q, we quantify the effect by the asymmetric ratio η_{CPD}, defined as

$$\eta_{\mathrm{CPD}} = \frac{\gamma^{\mathrm{L}} - \gamma^{\mathrm{R}}}{\gamma^{\mathrm{L}} + \gamma^{\mathrm{R}}} = -\frac{\gamma^{A}}{\gamma_{D}}. \tag{10}$$

Figure 2(a) puts this ratio on the same radial axis for the two Néel vector orientations, represented by $J = \pm 1.6\,\mathrm{eV}$. The sign reversal between the two curves is visible throughout the scanned radial range, consistent with the symmetry relation above. Along this cut, the signal is not a smooth function of $\boldsymbol{q}$: it exhibits a local peak at $q_1/k_{\mathrm{F,min}} = 0.2$ and a second, more pronounced peak with $|\eta_{\mathrm{CPD}}| \simeq 36\%$, at $q_2/k_{\mathrm{F,min}} = 0.55$, where $k_{\mathrm{F,min}} = \sqrt{\mu/(t + |J|/2)}$. Consequently, since η_{CPD} changes sign at any fixed momentum upon Néel vector reversal, measuring at a single momentum point is sufficient for detecting the switch.

To uncover the microscopic origin of this signal, we decompose γ^A into band-transition channels for $J = 1.6\,\mathrm{eV}$ in Fig. 3(a). The interband contribution $\gamma^A_{\mathrm{inter}}$ is visually indistinguishable from the total γ^A across the scan, with the intraband contribution staying below 10^{-4} of the peak. In this model, the CPD at each q therefore arises from interband coherent transitions between the spin-splitting branches; the leading intraband density-like term carries zero cross imaginary part and does not contribute to the net chiral response. Figures 3(b) and 3(c) show the $\boldsymbol{k}$-resolved kernel of γ^A at q_1 and q_2. We plot $\mathrm{sgn}(g_A)|g_A/g_{A,\max}|$, where $g_A(\boldsymbol{k},\boldsymbol{q})$ is the interband integrand of γ^A including all coefficients and $g_{A,\max}$ is its maximum absolute value within each panel. The kernel is shown on the SOC Fermi surface prior to

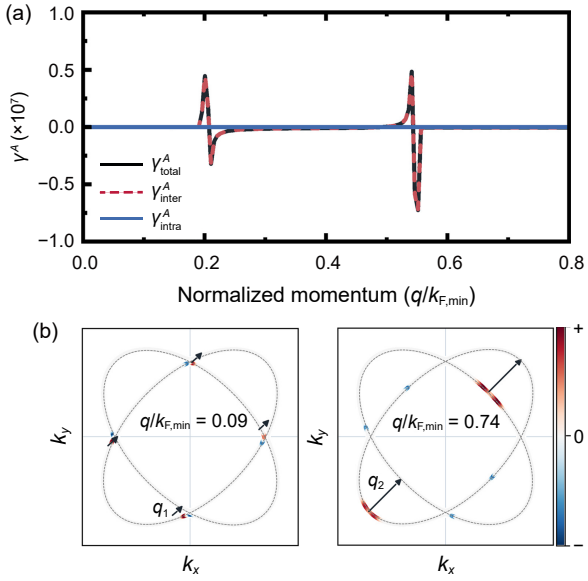

Fig. 3. Channel and k-resolved origin of the radial resonances. (a) Channel-resolved γ^A (1/s) for $J = 1.6\,\mathrm{eV}$: total (solid black), interband (dashed red), and intraband (solid blue). Interband kernel $g_A(\boldsymbol{k},\boldsymbol{q})$ of γ^A plotted as $\mathrm{sgn}(g_A)|g_A/g_{A,\max}|$ on the SOC Fermi surfaces for (b) $q_1/k_{\mathrm{F,min}} = 0.2$ and (c) $q_2/k_{\mathrm{F,min}} = 0.55$. Red and blue denote positive and negative values after separate panel normalization. Dashed lines show the SOC Fermi surfaces. Arrows indicate representative near-Fermi transitions $\boldsymbol{k}_i \to \boldsymbol{k}_i + \boldsymbol{q}_{1,2}$ selected by the corresponding peak momenta.

$\boldsymbol{k}$ integration, so the color encodes sign and relative weight within each panel. For q_1, four small regions near the crystalline axes carry the weight. For q_2, two larger patches dominate and are connected by the indicated finite-q transitions. The peaks originate from electron transitions due to the phonons at multiple regions near the Fermi surface. In the finite-q response, the energy conservation restricts the integrand to $\varepsilon_{s'}(\boldsymbol{k}+\boldsymbol{q}) - \varepsilon_s(\boldsymbol{k}) = \hbar\omega$. When this contour nearly touches a Fermi surface, or when its normal energy gradient becomes small, the joint density of states increases. Sweeping q then opens and closes resonant arcs and rearranges the positive and negative chiral weights. This produces both the peaks and the intervening zero crossings.

The radial cut establishes a representative signal scale and identifies a near-resonant momentum shell for angular readout. We therefore fix $|\boldsymbol{q}|/k_{\mathrm{F,min}} = 0.55$, slightly below the second peak to avoid numerical sensitivity at the exact resonance, and scan the propagation angle.

On this momentum shell, the angular scan reaches its largest absolute asymmetric ratio with $J = 1.6\,\mathrm{eV}$, $|\eta_{\mathrm{CPD}}| = 25\%$. Reversing the Néel vector (J to $-J$) reverses the entire angular curve up to numerical precision. The CPD also vanishes at $\phi_q = 0°$, $90°$, $180°$, and $270°$, consistent with the mirror symmetries M_x and M_y, which make the CPD odd under $q_x \to -q_x$ and $q_y \to -q_y$, respectively. Experimentally, the 2π-azimuthal scan shown in Fig. 4 can be realized with multiple shear-wave transducers placed at different azimuthal angles around the sample.

Beyond these symmetry-enforced zeros, the CPD changes sign additionally within each quadrant. These finite-angle lobes provide the practical readout points: once a resonant momentum shell is selected, the sign of the circular attenuation asymmetry distinguishes opposite Néel vector orientations. Thus symmetry fixes the Néel vector sign relation and the four axis zeros, whereas the heights and extra sign changes are controlled by the phonon assisted electron transitions with finite-momentum transfer. In addition, we also give the results of linear phonon dichroism in the SM.

We briefly discuss the relation between CPD and the Fermi-surface geometry and Néel vector. As illustrated in Fig. 3, CPD originates from interband transitions between spin-split bands. The two transition channels, up→down and down→up, contribute to η_{CPD}

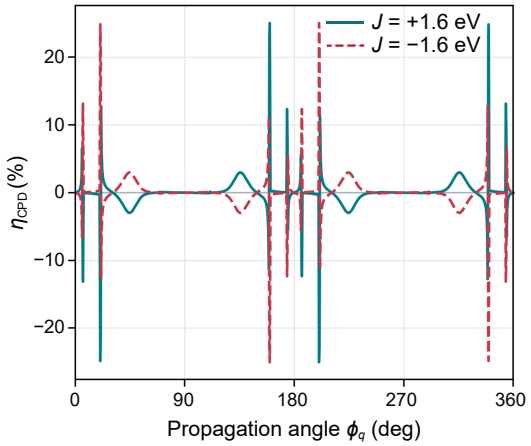

Fig. 4. Directional scan of the finite-momentum CPD for $J = \pm 1.6\,\mathrm{eV}$. The momentum magnitude is fixed at $|\boldsymbol{q}|/k_{\mathrm{F,min}} = 0.55$.

with opposite signs (see Fig. 4), so the sign and magnitude of η_{CPD} directly reflect the spin-splitting structure of the Fermi surface. In the d-wave altermagnet considered here, this leads to a characteristic four-fold angular dependence of η_{CPD}, which encodes the d-wave symmetry of the Fermi surface. The same analysis could be applicable to other altermagnets, such as f-wave and g-wave, where the corresponding angular dependence of η_{CPD} would reflect the specific Fermi-surface geometry. Furthermore, because CPD is sensitive to the spin splitting and its sign reverses upon reversing the Néel vector, it provides a potentially useful probe of both the Fermi-surface geometry and the magnetic order in altermagnets.

Experimentally, the pulse-echo ultrasound method provides a direct probe of CPD. The directly measured quantities are the incident amplitude A_0 and the two transmitted amplitudes A^{L} and A^{R}. For a sample of thickness d and sound velocity c_{t}, the damping rates satisfy $\gamma^{\mathrm{L/R}} = -(c_{\mathrm{t}}/d)\ln(A^{\mathrm{L/R}}/A_0)$ [77], so

$$\eta_{\mathrm{CPD}} = -\frac{\ln(A^{\mathrm{L}}/A^{\mathrm{R}})}{\ln\left[A_0^2/(A^{\mathrm{L}}A^{\mathrm{R}})\right]}. \tag{11}$$

Thus η_{CPD} is determined entirely by the measured amplitudes; no knowledge of d, c_{t}, or other material-specific parameters is required. For a typical transverse acoustic velocity $c_{\mathrm{t}} \sim 3\times10^3\,\mathrm{m/s}$ and the damping difference $\gamma^{\mathrm{L}} - \gamma^{\mathrm{R}} \sim 10^7\,\mathrm{s}^{-1}$ at $|\boldsymbol{q}|/k_{\mathrm{F,min}} = 0.55$, the attenuation difference is estimated to be on the order of $10^3\,\mathrm{m}^{-1}$ (roughly 8 dB/mm), which is well above the detection threshold of current ultrasonic technology [78]. The two opposite Néel vector orientations can be distinguished by the sign of the attenuation difference. We note that in 2D materials the in-plane and out-of-plane transverse modes are non-degenerate, so an injected circular wave splits into two linearly polarized components. However, CPD is a local absorption property and can also be probed by far-infrared optical spectroscopy without requiring the wave to maintain circular polarization, as demonstrated in a recent experiment [79]. Moreover, realistic effects such as finite temperature, disorder, and phonon damping are expected to reduce the peak amplitudes and broaden the sharp features in η_{CPD}. However, the sign reversal of η_{CPD} upon Néel vector reversal is symmetry-enforced and therefore remains robust. Thus, even with realistic broadening, the CPD signal provides an unambiguous signature of Néel vector switching.

Conclusions

We developed a finite-momentum theory of CPD for d-wave altermagnets and revealed its origin in the chiral interband matrix elements. Meanwhile, CPD is odd under Néel vector reversal and exhibits strong wave-vector modulation near resonant phonon momenta. Specifically, representative finite-momentum cuts show pronounced dichroic resonances: the radial cut reaches $|\eta_{\mathrm{CPD}}| = 36\%$, and the selected angular scan reaches $|\eta_{\mathrm{CPD}}| = 25\%$. Thus, our work provides an acoustic probe of the Néel vector in d-wave altermagnets, which can be straightforwardly extended to other altermagnetic materials.

Acknowledgements

This work was supported by the National Key R&D Program of the MOST of China (Grant No. 2024YFA1611300), the National Natural Science Foundation of China (Grant No. 12574059), HFIPS Director's Fund (Grant No. BJPY2023B05), Anhui Provincial Major S&T Project (Grant No. s202305a12020005), the Basic Research Program of the Chinese Academy of Sciences Based on Major Scientific Infrastructures (Grant No. JZHKYPT-2021-08), and the High Magnetic Field Laboratory of Anhui Province (Contract No. AHHM-FX-2020-02).

References

[1] Baltz V, Manchon A, Tsoi M, Moriyama T, Ono T, and Tserkovnyak Y 2018 *Rev. Mod. Phys.* **90** 015005
[2] Jungwirth T, Marti X, Wadley P, and Wunderlich J 2016 *Nat. Nanotechnol.* **11** 231
[3] Šmejkal L, Mokrousov Y, Yan B, and MacDonald A H 2018 *Nat. Phys.* **14** 242
[4] Němec P, Fiebig M, Kampfrath T, and Kimel A V 2018 *Nat. Phys.* **14** 229
[5] Yuan J K, Pan Z, and Wu C 2026 *Phys. Rev. B* **113** 014426
[6] Krempaský J, Šmejkal L, D'Souza S W *et al.* 2024 *Nature* **626** 517
[7] Šmejkal L, Sinova J, and Jungwirth T 2022 *Phys. Rev. X* **12** 031042
[8] Turek I 2022 *Phys. Rev. B* **106** 094432
[9] Bai L, Feng W, Liu S, Šmejkal L, Mokrousov Y, and Yao Y 2024 *Adv. Funct. Mater.* **34** 2409327
[10] González-Hernández R, Šmejkal L, Výborný K, Yahagi Y, Sinova J, Jungwirth T, and Železný J 2021 *Phys. Rev. Lett.* **126** 127701
[11] Šmejkal L, Hellenes A B, González-Hernández R, Sinova J, and Jungwirth T 2022 *Phys. Rev. X* **12** 011028
[12] Zhang Y, Bai H, Dai J, Han L, Chen C, Liang S, Cao Y, Zhang Y, Wang Q, Zhu W, Pan F, and Song C 2025 *Nat. Commun.* **16** 5646
[13] Qin P, Yan H, Wang X, Chen H, Meng Z, Dong J, Zhu M, Cai J, Feng Z, Zhou X, Liu L, Zhang T, Zeng Z, Zhang J, Jiang C, and Liu Z 2023 *Nature* **613** 485
[14] Zhu Y P, Chen X, Liu X R *et al.* 2024 *Nature* **626** 523
[15] Jang I, Aquino R, Schmalian J and Fernandes R M 2026 arXiv:2606.26239 [cond-mat.mes-hall]
[16] Liu L S, Shao K, Li H D, Wan X, Chen W, and Xing D Y 2026 *Phys. Rev. Lett.* **136** 106301
[17] Lin H J, Zhang S B, Lu H Z, and Xie X C 2025 *Phys. Rev. Lett.* **134** 136301
[18] Liu Y and Liu C C 2026 *Phys. Rev. Lett.* **136** 256709
[19] Liu D, Zhuang Z Y, Zhu D, Wu Z, and Yan Z 2026 *Phys. Rev. B* **113** L060409
[20] Bai H, Zhang Y C, Zhou Y J, Chen P, Wan C H, Han L, Zhu W X, Liang S X, Su Y C, Han X F, Pan F, and Song C 2023 *Phys. Rev. Lett.* **130** 216701
[21] Bhowal S and Spaldin N A 2024 *Phys. Rev. X* **14** 011019
[22] Jin Z, Zeng Z, Liu J, Gong T, Su Y, Chang K, and Yan P 2026 *Phys. Rev. Lett.* **136** 086703
[23] Monkman K, Weng J, Heinsdorf N, Nocera A, Barlas Y, and Franz M 2026 *Phys. Rev. X* **16** 011057
[24] González-Hernández R, Ritzinger P, Výborný K, Železný J, and Manchon A 2024 *Nat. Commun.* **15** 7663
[25] Yang Y, Wang D, Yang B, Wang P, Mu Y, Tian Y, Zheng B, Qin W, Wang K, Huang B, Wang B, Wan X, and Wu D 2026 *Phys. Rev. Lett.* **136** 026701
[26] Ding N, Ye H, Wang S S, and Dong S 2025 *Phys. Rev. B* **112** L220410
[27] Takagi R, Hirakida R, Settai Y *et al.* 2025 *Nat. Mater.* **24** 63
[28] Zhu Z, Huang R, Chen X, Cui Z, Duan X, Zhang J, Žutić I, and Zhou T 2026 *Phys. Rev. Lett.* **136** 186702
[29] Zhang S B, Hu L H, and Neupert T 2024 *Nat. Commun.* **15** 1801
[30] Wadley P, Howells B, Železný J *et al.* 2016 *Science* **351** 587
[31] Han L, Fu X, Peng R, Cheng X, Dai J, Liu L, Li Y, Zhang Y, Zhu W, Bai H, Zhou Y, Liang S, Chen C, Wang Q, Chen X, Yang L, Zhang Y,

Song C, Liu J, and Pan F 2024 *Sci. Adv.* **10** eadn0479
[32] Godinho J, Reichlová H, Kriegner D, Novák V, Olejník K, Kašpar Z, Šobáň Z, Wadley P, Campion R P, Otxoa R M, Roy P E, Železný J, Jungwirth T, and Wunderlich J 2018 *Nat. Commun.* **9** 4686
[33] Saidl V, Němec P, Wadley P, Hills V, Campion R P, Novák V, Edmonds K W, Maccherozzi F, Dhesi S S, Gallagher B L, Trojánek F, Kuneš J, Železný J, Malý P, and Jungwirth T 2017 *Nat. Photonics* **11** 91
[34] Xiao R C, Li H, Han H, Gan W, Yang M, Shao D F, Zhang S H, Gao Y, Tian M, and Zhou J 2026 *Sci. China Phys. Mech. Astron.* **69** 217511
[35] Chen R, Wang Z M, Wu K, Sun H P, Zhou B, Wang R, and Xu D H 2025 *Phys. Rev. Lett.* **135** 096602
[36] Dong R, Xiao Y, and Fei R 2026 *Phys. Rev. Lett.* **136** 216702
[37] Fang Y, Cano J, and Ghorashi S A A 2024 *Phys. Rev. Lett.* **133** 106701
[38] Pan H, Xiao R C, Han J, Zhu H, Li J, Niu Q, Gao Y, and Hou D 2026 *Phys. Rev. Lett.* **136** 036701
[39] Luo J, Zhou X, Liang J, Wang L, Zhou Q, Jiang Y, Wang W, Yao Y, Yang L, and Jiang W 2026 *Chin. Phys. Lett.* **43** 020713
[40] Zhang L and Niu Q 2014 *Phys. Rev. Lett.* **112** 085503
[41] Juraschek D M, Geilhufe R M, Zhu H *et al*. 2025 *Nat. Phys.* **21** 1532
[42] Zhang T and Murakami S 2022 *Phys. Rev. Res.* **4** L012024
[43] Liu D and Shi J 2017 *Phys. Rev. Lett.* **119** 075301
[44] Shan W Y 2022 *Phys. Rev. B* **105** L121302
[45] Li D, Yang G, Qin T, Zhou J, and Yao Y 2025 arXiv:2511.16141 [cond-mat.mes-hall]
[46] Xiao D, Chang M C, and Niu Q 2010 *Rev. Mod. Phys.* **82** 1959
[47] Berry M V 1984 *Proc. R. Soc. Lond. A* **392** 45
[48] Kuneš J 2025 *Phys. Rev. B* **112** 184415
[49] Ezawa M 2024 *Phys. Rev. B* **110** L241405
[50] Nolting W and Brewer W D 2009 *Fundamentals of Many-body Physics* (Berlin: Springer)
[51] Mahan G D 2020 *Many-Particle Physics* (New York: Springer)
[52] Shan W Y 2023 *Phys. Rev. Res.* **5** L022038
[53] Qin T, Zhou J, and Shi J 2012 *Phys. Rev. B* **86** 104305
[54] Zhang L and Niu Q 2015 *Phys. Rev. Lett.* **115** 115502
[55] Chen Y, Qin W, Zhang S, Cui P, Niu Q, and Zhang Z 2025 *Phys. Rev. Lett.* **135** 126608
[56] Zhang S, Huang Z, Du M, Ying T, Du L, and Zhang T 2026 *Phys. Rev. B* **113** 024302
[57] de Juan F, Sturla M, and Vozmediano M A H 2012 *Phys. Rev. Lett.* **108** 227205
[58] de Juan F, Mañes J L, and Vozmediano M A H 2013 *Phys. Rev. B* **87** 165131
[59] Pereira V M and Neto A H C 2009 *Phys. Rev. Lett.* **103** 046801
[60] Mañes J L 2007 *Phys. Rev. B* **76** 045430
[61] Kleiner W H 1966 *Phys. Rev.* **142** 318
[62] Rao P, Mook A, and Knolle J 2024 *Phys. Rev. B* **110** 024425
[63] Chen W, Zhou X, Lou W K, and Chang K 2025 *Phys. Rev. B* **111** 064428
[64] Resta R 2020 *Phys. Rev. Res.* **2** 023139
[65] Lai J, Yu T, Liu P, Liu L, Xing G, Chen X Q, and Sun Y 2025 *Phys. Rev. Lett.* **135** 256702
[66] Fedchenko O, Minár J, Akashdeep A *et al*. 2024 *Sci. Adv.* **10** eadj4883
[67] Šmejkal L, González-Hernández R, Jungwirth T, and Sinova J 2020 *Sci. Adv.* **6** eaaz8809
[68] Jiang B, Hu M, Bai J, Song Z, Mu C, Qu G, Li W, Zhu W, Pi H, Wei Z, Sun Y J, Huang Y, Zheng X, Peng Y, He L, Li S, Luo J, Li Z, Chen G, Li H, Weng H, and Qian T 2025 *Nat. Phys.* **21** 754
[69] Roig M, Kreisel A, Yu Y, Andersen B M, and Agterberg D F 2024 *Phys. Rev. B* **110** 144412
[70] Bychkov Y A and Rashba É I 1985 *Sov. Phys. Usp.* **28** 632
[71] Nagaosa N, Sinova J, Onoda S, MacDonald A H, and Ong N P 2010 *Rev. Mod. Phys.* **82** 1539
[72] Nomura T, Zhang X X, Zherlitsyn S, Wosnitza J, Tokura Y, Nagaosa N, and Seki S 2019 *Phys. Rev. Lett.* **122** 145901
[73] Weißenhofer M, Rieger P, Mrudul M S, Mikadze L, Nowak U, and Oppeneer P M 2025 *Phys. Rev. Lett.* **135** 216701
[74] Xiao Z, Zhao J, Li Y, Shindou R, and Song Z D 2024 *Phys. Rev. X* **14** 031037
[75] Watanabe H, Shinohara K, Nomoto T, Togo A, and Arita R 2024 *Phys. Rev. B* **109** 094438
[76] Chen X, Ren J, Zhu Y, Yu Y, Zhang A, Liu P, Li J, Liu Y, Li C, and Liu Q 2024 *Phys. Rev. X* **14** 031038
[77] Schmerr L W 2016 *Fundamentals of Ultrasonic Nondestructive Evaluation* (Cham: Springer)
[78] Woodruff T O and Ehrenreich H 1961 *Phys. Rev.* **123** 1553
[79] Yang R, Zhu Y Y, Steigleder M, Liu Y C, Liu C C, Qiu X G, Zhang T, and Dressel M 2025 *Phys. Rev. Lett.* **134** 196905